Hydrodynamic performance of the dual-chamber oscillating water column device placed over the undulated sea bed

Kshma Trivedi, Santanu Koley[*]

Department of Mathematics, Birla Institute of Technology & Science-Pilani, Hyderabad Campus, Telangana 500078, India

Abstract

The present study analyzed the efficiency of the dual-chamber oscillating water column device placed over the undulated bottom. The efficiency of the device is studied for various shape parameters such as chamber lengths, the draft of the lip wall of the device, turbine damping coefficients, and ripples of the corrugated bottom. It is seen that the efficiency initially increases as the wavenumber increases. However, the efficiency of the device becomes lower for shorter incident wavelength. The amplitude of the resonance becomes higher for device having wider chamber. Similar higher resonance occurs when the turbine damping coefficients and the number of ripples of the corrugated bottom take higher values. An opposite pattern is formed with the variation in draft of the lip wall of the device. The draft of the outer chamber plays a dominant role in enhancing the efficiency as compared to the draft of the inner chamber of the device. Further, the efficiency becomes higher as the turbine damping coefficient takes the higher values.

1. Introduction

The global energy debate is currently focused on energy supplies, the consequences of their exhaustion, and price fluctuations. It is imperative to find some promising sustainable renewable energy resources to alleviate the global crisis. Due to numerous advantages such as abundant resources and low environmental impact, wave energy has become one of the prevalent renewable energy sources, and its privileges and implementation features are also steadily upgraded [1]. Among the various WECs, the OWC-WEC device is mostly used and has numerous benefits over the other WEC devices. Rezanejad et al. [2] explored the functioning of the duplex OWC-WEC placed over the seabed having multiple steps. The results revealed that the presence of a step seabed before the OWC-WEC significantly increases the device' efficiency. Further, Rezanejad et al. [3] extended the work of Rezanejad et al.

---

* Corresponding author.
  E-mail address: santanu@hyderabad.bits-pilani.ac.in (S. Koley).

[2] by incorporating the multi-chamber OWC-WEC placed over flat seabed. The outcomes of the study shows that the draft of the lip wall of the outer OWC-WEC chamber remarkably amplifies the efficiency when compared with the immersion depth of the inner chambers. He et al. [4] performed model tests to demonstrate the operational mechanism of the floating OWC-WEC having double chambers, and drew the following conclusions: (i) the shape parameters of the front chamber of the OWC-WEC should be chosen appropriately for maximum energy absorption, (ii) the narrower-chamber width noticeably enhances the oscillation within the OWC-WEC chamber, which leads to the higher amount of power extraction. Ning et al. [5] used HOBEM to investigate the effect of shape parameters on the functioning of duplex OWC-WEC using time-domain analysis. It was observed that the water surface oscillation within the dual-chamber was largely affected by the incident wave conditions. Elhanafi et al. [6] utilized the CFD tool to investigate the working mechanism of a solo chamber as duplex type OWC-WEC. It was observed that for long and intermediate incident wavelengths, the capacity of power generation of the duplex type OWC-WEC is more as compared to the single-chamber OWC-WEC. Shalby et al. [7] extended the work of Elhanafi et al. [6] to the case of multi-chamber OWC-WEC, and obtained the following conclusions: (i) differential air pressure strongly depends on the PTO damping, and (ii) free surface elevation and airflow rate decrease with an increase in PTO damping. Howe et al. [8] analyzed the sequel of structural shape on the working mechanism of floating breakwater integrated multi-chamber OWC-WEC experimentally. It was observed that the structural configuration and chamber spacing significantly impact the performance of a multi-chamber OWC. Wan et al. [9] investigated the efficiency of the breakwater integrated dual-cylindrical OWC-WEC, and obtained the following conclusions: (i) the water surface displacement within the OWC-WEC chamber increases as the time-period increases and attains maximum. Hereafter, the water surface displacement within the OWC-WEC chamber decreases for further increase in time-period. (ii) For long incident waves, the conversion efficiency of the OWC-WEC strongly controlled by the baffle angle and relative diameter as the wavenumber increases, and (iii) diameter ratio plays a crucial role to improve the performance of an OWC-WEC as compared to the baffle angle. Recently, Zhou et al. [10] used HOBEM to study the functioning of multi OWC-WECs using time-domain analysis. It was found that the efficiency of multi OWC-WEC devices steadily affected by the gap length between the OWC-WECs.

The present research focuses on the performance of the dual-chamber OWC-WEC. The overall organization of this paper is as follows. Firstly, the analogous BVP is described. Thereafter, the DBEM (dual boundary element method) based solutions are given. Various parameters related with the functionality of the OWC are highlighted in Section 4. Finally, the results and summary are given in Sections 5 and 6 respectively.

2. BVP formulation

This section contains the mathematical modeling of the dual-chamber OWC. For modeling purpose, the 2D Cartesian coordinate system is taken. The OWC-WEC comprises of an impenetrable seaside wall at $x = L - (b_1 + b_2)$ and has draft a_1. Further, the rear-side wall is positioned at $x = L$. The OWC-WEC consists of dual chambers with chamber lengths b_1 and b_2 respectively, and separating by a vertical wall with draft a_2. Further, the device is situated over the corrugated bottom $z = -h(x)$. The corrugated seabed is finitely extended as shown is Fig. 1. Moreover, Γ_f represents the external free surface occupies the region $\Gamma_f = \{(x, z): z = 0, -\infty < x < L - (b_1 + b_2)\}$. On the other hand, Γ_{b1} and Γ_{b2} are the internal free surfaces occupy the regions $\Gamma_{b1} = \{(x, z): z = 0, L - (b_1 + b_2) < x < L - b_2\}$ and $\Gamma_{b2} = \{(x, z): z = 0, L - b_2 < x < L\}$ respectively. Further, Γ_b, Γ_L, $\Gamma_{a1}^{\pm}$, and $\Gamma_{a2}^{\pm}$ are the impenetrable boundaries of the dual-chamber OWC-WEC as seen in Fig. 1. Further, a fictitious boundary Γ_l is constructed at $x = -l$ to satisfy the far-field boundary condition. For the sake of modeling, the water flow follows the linear flow theory and related motion is time harmonic. The velocity potential is given by $\psi(x, z, t) = \Re\{\varphi(x, z)e^{-i\sigma t}\}$. With this framework, the governing equation is

$$\nabla^2 \varphi(x, z) = 0. \tag{1}$$

Due to the presence of an OWC-WEC, the velocity potential φ can be decomposed as

$$\varphi = \varphi^S + \left(\frac{i\sigma p_1}{\rho g}\right)\varphi^{R1} + \left(\frac{i\sigma p_2}{\rho g}\right)\varphi^{R2}, \tag{2}$$

where, φ^S is termed as scattered potential, φ^{R1} and φ^{R2} are related to the radiated potentials associated with the front and rear chamber respectively. Further, p_1 and p_2 represent the distribution of pressure within the front and
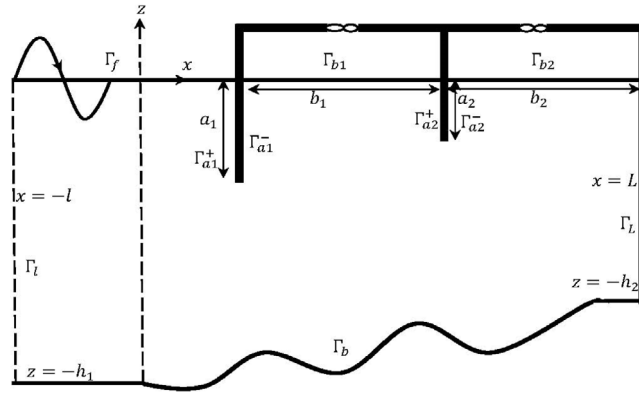
Fig. 1. Sideview of the dual-chamber OWC-WEC.

rear chamber respectively. The free surface bcs (boundary conditions) at $z = 0$ are given by (see [11])

$$\frac{\partial \varphi^{R1}}{\partial n} - K\varphi^{R1} = \begin{cases} \dfrac{i\omega p_1}{\rho g}, & \text{on } \Gamma_{b1}, \\ 0, & \text{on } \Gamma_{b2} \cup \Gamma_f. \end{cases} \tag{3}$$

$$\frac{\partial \varphi^{R2}}{\partial n} - K\varphi^{R2} = \begin{cases} \dfrac{i\omega p_2}{\rho g}, & \text{on } \Gamma_{b2}, \\ 0, & \text{on } \Gamma_{b1} \cup \Gamma_f. \end{cases} \tag{4}$$

$$\frac{\partial \varphi^{S}}{\partial n} - K\varphi^{S} = 0, \text{ on } \Gamma_{b1} \cup \Gamma_{b2} \cup \Gamma_f. \tag{5}$$

Here, $K = \frac{\sigma^2}{g}$. Now, the bc on the impenetrable bottom Γ_b is represented as

$$\frac{\partial \varphi^{S,Rj}}{\partial n} = 0, \text{ on } \Gamma_b (\text{for } j = 1, 2). \tag{6}$$

Similarly, the bcs on the impenetrable boundaries $\Gamma_L \cup \Gamma_{a1}^{\pm} \cup \Gamma_{a2}^{\pm}$ are given by

$$\frac{\partial \varphi^{S,Rj}}{\partial n} = 0, \text{ on } \Gamma_L \cup \Gamma_{a1}^{\pm} \cup \Gamma_{a2}^{\pm} (\text{for } j = 1, 2). \tag{7}$$

Finally, the far-field boundary condition at Γ_l can be written as

$$\frac{\partial \varphi^{S,Rj}}{\partial n} - ik_0 \varphi^{S,Rj} = \Xi \left(\frac{\partial \varphi^{inc}}{\partial n} - ik_0 \varphi^{inc} \right), \text{ on } \Gamma_l (\text{for } j = 1, 2). \tag{8}$$

Here, $\Xi = 1$ for φ^S and $\Xi = 0$ for $\varphi^{Rj}(j = 1, 2)$. Further, k_0 satisfies the dispersion equation $\omega^2 = gk \tanh(kh_1)$.

3. Solution methodology

In the present section, DBEM is used to obtain the solution of the BVP as written before. Using Green's identity on $\varphi^{S,Rj}(j = 1, 2)$ and the unbounded Green's function $\tilde{G}(\tilde{x}, \tilde{s})$, the following Fredholm integral equations are obtained

$$2\pi \varphi^{S,Rj}(\tilde{x}) = \int_{\Gamma} \frac{\partial \tilde{G}(\tilde{s}, \tilde{x})}{\partial n_{\tilde{s}}} \varphi^{S,Rj}(\tilde{s}) d\Gamma(\tilde{s}) - \int_{\Gamma} \tilde{G}(\tilde{s}, \tilde{x}) \frac{\partial \varphi^{S,Rj}(\tilde{s})}{\partial n_{\tilde{s}}} d\Gamma(\tilde{s}), \tilde{x} \in \Omega \ (j = 1, 2). \tag{9}$$

Here, $\tilde{s} = (\varsigma, \mu)$ and $\tilde{x} = (x, z)$ are the source and field points respectively. The free space Green's function takes the form (for normal incident waves)

$$\tilde{G}(\tilde{x}, \tilde{s}) = \ln \tilde{r}, \qquad \tilde{r} = \sqrt{(x - \varsigma)^2 + (z - \mu)^2}. \tag{10}$$

Now, taking normal derivative, Eq. (9) yields

$$2\pi \frac{\partial \varphi^{S,Rj}(\tilde{x})}{\partial n_{\tilde{x}}} = \int_{\Gamma} \frac{\partial^2 \tilde{G}(\tilde{s},\tilde{x})}{\partial n_{\tilde{s}}\partial n_{\tilde{x}}} \varphi^{S,Rj}(\tilde{s}) d\Gamma(\tilde{s}) - \int_{\Gamma} \frac{\partial \tilde{G}(\tilde{s},\tilde{x})}{\partial n_{\tilde{x}}} \frac{\partial \varphi^{S,Rj}(\tilde{s})}{\partial n_{\tilde{s}}} d\Gamma(\tilde{s}), \tilde{x} \in \Omega \ (j=1,2). \tag{11}$$

When $\tilde{x} \in \Gamma$, Eqs. (9) and (11) can be expressed as

$$\pi \varphi^{S,Rj}(\tilde{x}) = \text{CPV} \int_{\Gamma} \frac{\partial \tilde{G}(\tilde{s},\tilde{x})}{\partial n_{\tilde{s}}} \varphi^{S,Rj}(\tilde{s}) d\Gamma(\tilde{s}) - \text{RPV} \int_{\Gamma} \tilde{G}(\tilde{s},\tilde{x}) \frac{\partial \varphi^{S,Rj}(\tilde{s})}{\partial n_{\tilde{s}}} d\Gamma(\tilde{s}), \tilde{x} \in \Gamma \ (j=1,2), \tag{12}$$

$$\pi \frac{\partial \varphi^{S,Rj}(\tilde{x})}{\partial n_{\tilde{x}}} = \text{HPV} \int_{\Gamma} \frac{\partial^2 \tilde{G}(\tilde{s},\tilde{x})}{\partial n_{\tilde{s}}\partial n_{\tilde{x}}} \varphi^{S,Rj}(\tilde{s}) d\Gamma(\tilde{s}) - \text{CPV} \int_{\Gamma} \frac{\partial \tilde{G}(\tilde{s},\tilde{x})}{\partial n_{\tilde{x}}} \frac{\partial \varphi^{S,Rj}(\tilde{s})}{\partial n_{\tilde{s}}} d\Gamma(\tilde{s}), \tilde{x} \in \Gamma \ (j=1,2). \tag{13}$$

Here, CPV, HPV, and RPV are termed as Cauchy, Hadamard and Riemann principal values respectively. In Eqs. (12) and (13), the total boundary $\Gamma = \Gamma_C + \Gamma_{a1}^{\pm} + \Gamma_{a2}^{\pm}$ with $\Gamma_C = \Gamma_l + \Gamma_L + \Gamma_b + \Gamma_{b1} + \Gamma_{b2} + \Gamma_f$ being the non-degenerate boundary and $\Gamma_{a1}^{\pm}$ and $\Gamma_{a2}^{\pm}$ are termed as degenerate boundaries respectively. Now, a number of integral equations are derived from Eqs. (12) and (13) by choosing $\tilde{x} \in \Gamma_C$, and $\tilde{x} \in \Gamma_{a1}^{\pm} \cup \Gamma_{a2}^{\pm}$. These systems of integral equations are transformed into algebraic equations and solved them to obtain the required unknowns. The details are provided in [12] and are deferred here.

4. Various coefficients related to the performance of the OWC-WEC

Here, various coefficients related to the performance of the OWC are given. The average energy flux per unit length is given as (see [13] for details)

$$\tilde{P}_W = E C_g = \frac{\rho \omega k_0 \tilde{A}_0}{2}, \ \tilde{A}_0 = \frac{2k_0 h_1 + \sinh(2k_0 h_1)}{4k_0 \cosh^2(k_0 h_1)}. \tag{14}$$

Here, C_g and E are termed as group velocity and total energy per unit wave period respectively. Now, the mean power extracted $\tilde{W}_w$ per unit width of pressure distribution is calculated using

$$\tilde{W}_w = \frac{1}{2} \Lambda_1 |p_1|^2 + \frac{1}{2} \Lambda_2 |p_2|^2, \tag{15}$$

where, Λ_1 and Λ_2 are control parameters of the turbines of the lip and rear chambers respectively. Finally, the OWC's efficiency is provided as

$$\tilde{\eta} = \frac{\tilde{W}_w}{\tilde{P}_w}. \tag{16}$$

5. Results

The parameters associated with waves and OWC are the following: $h_1 = 15$ m, $h_2 = h_1/1.5$, $L = 2.0h_1$, $b_1 = b_2 = 0.5h_1$, $a_1/h_1 = 0.4$, $\Lambda_1 = 1.609 \times 10^{-4}$ m^4 s/kg, $\Lambda_2 = 0.885 \times 10^{-4}$ m^{4}s/kg unless otherwise mentioned.

Bottom profile : $\Gamma_b = -\left\{ h_2 + H \left(1 + 2 \left(\frac{x}{L}\right)^3 - 3 \left(\frac{x}{L}\right)^2 - \left(\frac{a}{H}\right) \sin\left(\frac{2m\pi x}{L}\right) \right) \right\}$,

where, $H = h_1 - h_2$, a and m represent the ripple magnitude and the ripples number respectively.

Firstly, a comparison between the present results and the outcome of Rezanejad et al. [2] is provided. To adopt the OWC device model of Rezanejad et al. [2], the limiting case is taken $a_1 = 8$ m, $a_2 = 0.5$ m, $b_1 = 9$ m, $b_2 = 12$ m, $h_1 = 10$ m, $h_2 = 10$ m. Fig. 2 demonstrates the variation of $\tilde{\eta}_{max}$ as a function of time period. The comparison shows that the present results match well with Rezanejad et al. [2].

Figs. 3(a) and 3(b) describe the change of $\tilde{\eta}$ versus dimensionless wavenumber Kh_1 for various chamber lengths $\frac{b_1}{h_1}$ and $\frac{b_2}{h_2}$, and the draft $\frac{a_1}{h_1}$ of the lip wall of the device respectively. In Fig. 3(a), the efficiency $\tilde{\eta}$ of the dual chamber OWC-WEC initially takes higher values as the wavenumber Kh_1 becomes higher and attains maximum. Hereafter, $\tilde{\eta}$ becomes lower for further decrease in incident wavelength. Further, for long incident waves, the resonance amplitude is higher for higher $\frac{b_1}{h_1}$ and $\frac{b_2}{h_2}$. Moreover, a small drop is seen in the $\tilde{\eta}$ curve for higher values of $\frac{b_1}{h_1}$ and $\frac{b_2}{h_2}$ in the intermediate and shortwave regime. In Fig. 3(b), the efficiency $\tilde{\eta}$ of the device increases as the wavenumber Kh_1
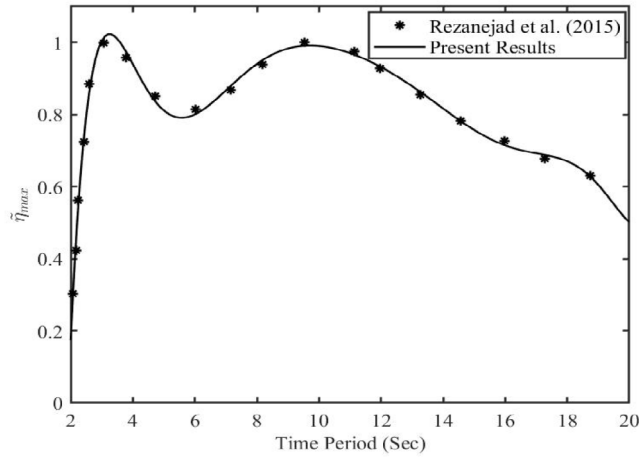
Fig. 2. Comparison of present results with Rezanejad et al. [2] for $\tilde{\eta}_{max}$ vs T.
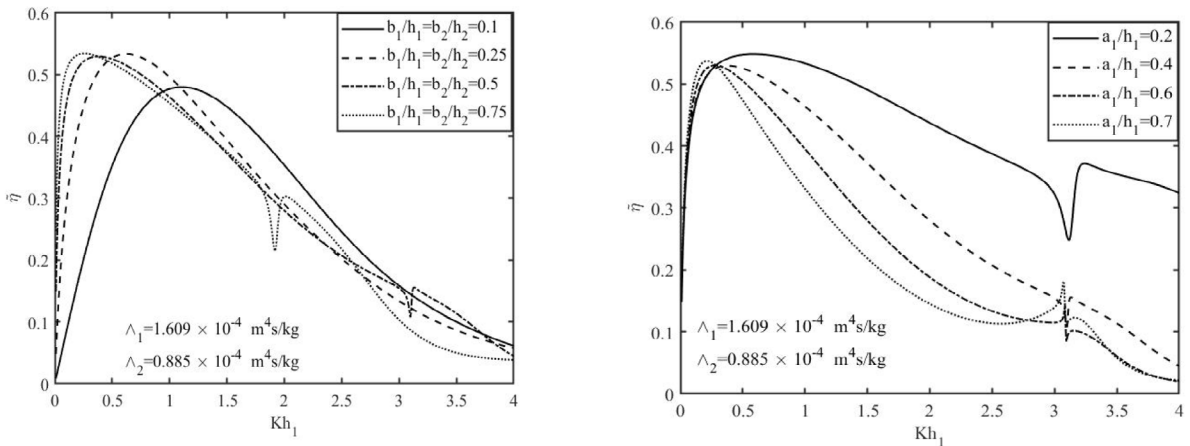

Fig. 3. $\tilde{\eta}$ vs Kh_1 for various (a) chamber lengths $\frac{b_1}{h_1}$ and $\frac{b_2}{h_2}$ (b) draft $\frac{a_1}{h_1}$.

becomes higher for long incident wave case. Further, the efficiency $\tilde{\eta}$ takes higher values for $\frac{a_1}{h_1} = 0.2$. In addition, a sharp peak is obtained at $Kh_1 \approx 3.0$ for higher values of draft $\frac{a_1}{h_1}$. Moreover, the efficiency $\tilde{\eta}$ has a small drop for smaller values of $\frac{a_1}{h_1}$ in the shortwave regime. These phenomena are related with the resonance mechanisms of the OWCs (see [14] for details). These results indicate that the chamber lengths and draft of the lip wall play a key role to enhance the performance of the OWC-WEC.

Figs. 4(a) and 4(b) demonstrate the changes of $\tilde{\eta}$ due to the change in Kh_1 for different damping coefficients Λ_1 and Λ_2 and for the different number of ripples m respectively. In Fig. 4(a), it is noticed that the pattern of the resonance is similar to that of Fig. 3(a). Further, it is observed that the resonance in the $\tilde{\eta}$ curve is higher for the positive values of turbine damping coefficients for long incident waves case. Moreover, in the shortwave regime, a sharp peak is observed in the efficiency curve for the turbine damping coefficient $\Lambda_2 = 0$, and the efficiency curve has a small drop for nonzero turbine damping coefficients. A similar pattern is also observed for the zero value of the front chamber's turbine damping coefficient. In Fig. 4(b), the overall pattern of resonance is similar to that of Fig. 3(a). Further, for long incident waves, the amplitude of the resonance in the $\tilde{\eta}$ curve is higher for sinusoidal seabed with higher number of ripples m. However, no significant variation is observed in the intermediate and shortwave regimes. These results show that the turbine damping coefficients and seabed variations significantly impact the efficiency of the OWC-WEC. The aforementioned observations are similar as that of Rezanejad et al.
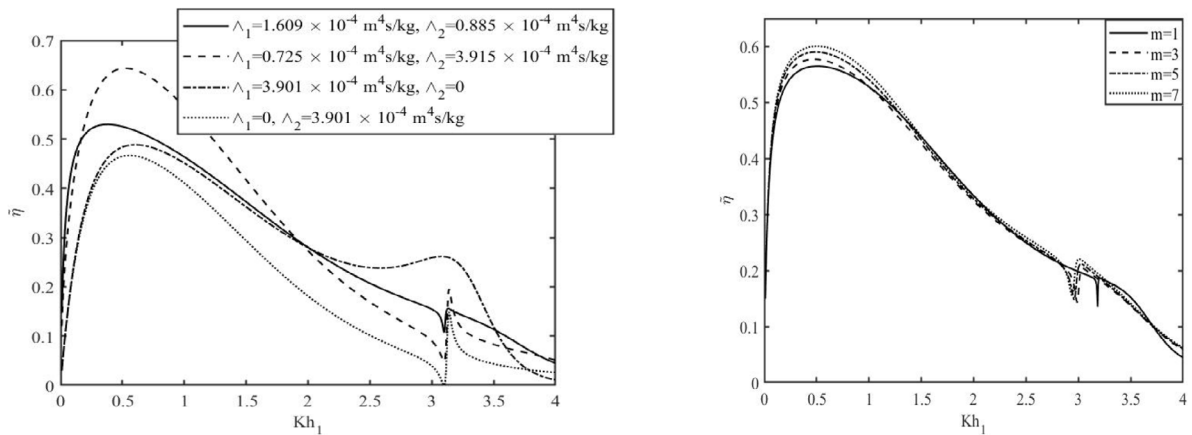
Fig. 4. $\tilde{\eta}$ vs Kh_1 for various (a) turbine damping coefficients Λ_1 and Λ_2, and (b) number of ripples m.

[2] except the occurrences of resonance of for higher wavenumber. This occurs because of seabed undulation which was not there in [2] for the stepped type bottom profile.

6. Conclusions

In this study, the efficiency of a dual-chamber OWC-WEC placed over the undulated bed is examined for various wave and shape parameters. It is revealed that the efficiency of the device initially increases as the incident wavenumber becomes higher. Hereafter, the efficiency of the device becomes lower for shorter incident wavelength. A similar resonance characteristic occurs with the variation in the draft of the lip wall, turbine damping coefficients, and the ripples number of the corrugated seabed. Further, in the intermediate and shortwave regime, the efficiency curve has a small drop for the higher values of chamber lengths and the ripples number of the corrugated seabed. Moreover, a reverse pattern is seen with the variation in the draft of the lip wall of the dual-chamber OWC-WEC and the turbine damping coefficients. In addition, the efficiency curve has a small drop for the nonzero values of turbine damping coefficients as well as for the zero values of the turbine damping coefficient of the front chamber. On the other hand, a small peak is observed for the zero values of the turbine damping coefficient of the rear chamber. It is seen that the draft of the outer chamber plays a significant role in enhancing the efficiency as compared to the draft of the inner chamber of the device. Moreover, the efficiency becomes higher as the turbine damping coefficient takes the higher values. These results demonstrated that with suitable combinations of turbine characteristics and chamber dimensions, the efficiency can be enhanced significantly. The present solution technique based on DBEM can be used to investigate the performance of multi-chamber OWC device having complex structural configurations. The present research is based on the assumption of linear wave-structure interaction theory. In near future, a similar approach can be used to investigate the impact of non-linearities present in the waves and structures on the efficiency of the OWC device.

Declaration of competing interest

The authors declare that they have no known competing financial interests or personal relationships that could have appeared to influence the work reported in this paper.

Acknowledgments

References

[1] Wang Chen, Zhang Yongliang. Wave power extraction analysis for an oscillating water column device with various surging lip-walls. Ocean Eng 2021;220:108483.

[2] Rezanejad Kourosh, Bhattacharjee Joydip, Soares Carlos Guedes. Analytical and numerical study of dual-chamber oscillating water columns on stepped bottom. Renew Energy 2015;75:272–82.

[3] Rezanejad Kourosh, Bhattacharjee Joydip, Soares Carlos Guedes. Analytical and numerical study of nearshore multiple oscillating water columns. J Offshore Mech Arct Eng 2016;138(2).

[4] He Fang, Leng Jie, Zhao Xizeng. An experimental investigation into the wave power extraction of a floating box-type breakwater with dual pneumatic chambers. Appl Ocean Res 2017;67:21–30.

[5] Ning Dezhi, Wang Rongquan, Zhang Chongwei. Numerical simulation of a dual-chamber oscillating water column wave energy converter. Sustainability 2017;9(9):1599.

[6] Elhanafi Ahmed, Macfarlane Gregor, Ning Dezhi. Hydrodynamic performance of single–chamber and dual–chamber offshore–stationary oscillating water column devices using CFD. Appl Energy 2018;228:82–96.

[7] Shalby Mohammad, Elhanafi Ahmed, Walker Paul, Dorrell David G. CFD modelling of a small–scale fixed multi–chamber OWC device. Appl Ocean Res 2019;88:37–47.

[8] Howe Damon, Nader Jean-Roch, Macfarlane Gregor. Experimental investigation of multiple oscillating water column wave energy converters integrated in a floating breakwater: Energy extraction performance. Appl Ocean Res 2020;97:102086.

[9] Wan Chang, Yang Can, Fang Qinghe, You Zaijin, Geng Jing, Wang Yongxue. Hydrodynamic investigation of a dual-cylindrical OWC wave energy converter integrated into a fixed caisson breakwater. Energies 2020;13(4):896.

[10] Zhou Yu, Ning Dezhi, Chen Lifen, Iglesias Gregorio. Nonlinear hydrodynamic modeling of an offshore stationary multi-oscillating water column platform. Ocean Eng 2021;227:108919.

[11] Wang Chen, Zhang Yongliang. Wave power extraction analysis on a dual-chamber oscillating water column device composed by two separated units: An analytical study. Appl Ocean Res 2021;111:102634.

[12] Trivedi Kshma, Santanu Koley, Panduranga Kottala. Performance of an U-shaped oscillating water column wave energy converter device under oblique incident waves. Fluids 2021;6(4):137.

[13] Trivedi Kshma, Santanu Koley. Mathematical modeling of breakwater-integrated oscillating water column wave energy converter devices under irregular incident waves. Renew Energy 2021.

[14] Koley Santanu, Kshma Trivedi. Mathematical modeling of oscillating water column wave energy converter devices over the undulated sea bed. Eng Anal Bound Elem 2020;117:26–40.